# Nonreciprocity in millimeter wave devices using a magnetic grating metamaterial

Markus Tyboroski,[1] Rair Macêdo,[2,1,*] and Robert E. Camley[1]

[1]*Center for Magnetism and Magnetic Materials, Department of Physics and Energy Science, University of Colorado at Colorado Springs, Colorado Springs, Colorado 80918, USA*

[2]*James Watt School of Engineering, Electronics & Nanoscale Engineering Division, University of Glasgow, Glasgow G12 8QQ, United Kingdom*

(Received 6 August 2021; accepted 19 October 2021; published 12 November 2021)

The control and manipulation of many of light's fundamental properties, such as reflectivity, has become a topic of increasing interest since the advent of engineered electromagnetic structures—now known as metamaterials. Many of these metamaterial structures are based on the properties of dielectric materials. Magnetic materials, on the other hand, have long been known to interact with electromagnetic waves in unusual ways; in particular, their nonreciprocal properties have enabled rapid advances in millimeter wave technology. Here, we show how a structured magnetic grating can be employed to engineer electromagnetic response at frequencies upwards of hundreds of gigahertz. In particular, we investigate how nonreciprocal reflection can be induced and controlled in this spectral region through the composition of the magnetic grating. Moreover, we find that both surface and guided polaritons contribute to high-frequency nonreciprocity; the nature of these is also investigated. Control of electromagnetic radiation at high frequencies is a current challenge of communications technology where our magnetic gradient might be employed in devices including signal processing filters and unidirectional isolators.

DOI: 10.1103/PhysRevMaterials.5.115201

## I. INTRODUCTION

Magnetic materials have long been used for a variety of microwave applications including circulators and isolators for radar systems and mobile telephone relay stations [1,2]. Some of the main properties of magnets that enable such versatility are their negative effective permeability [3–5] and nonreciprocal response [3,6] near their ferromagnetic resonance frequency. This means that their electromagnetic characteristics depend on the direction of motion of the wave crossing through them. For just as long, ferrites and garnets—in particular, yttrium iron garnet (YIG)—have been the first-choice materials for most of these applications [7,8]. The interest in this class of materials stems from their typical operating frequency in the low gigahertz-frequency range, their low damping, as well as their nonmetallic behavior.

With the advent of new information technologies, such as 5G and even 6G, high-frequency bands—from the high gigahertz to the terahertz range—are now being considered in order to enable data rates on the order of hundreds of gigabits per second [9]. Thus, making it now necessary to develop new high-frequency operating devices [10], including on-chip terahertz isolators [11], amplifiers, and oscillators [12]. This brings about three main drawbacks when incorporating magnetic materials into electronic devices:

(1) The aforementioned class of materials is no longer the obvious choice as they would require extremely large applied magnetic fields in order to obtain such high operating frequencies [6,13,14];

(2) antiferromagnetic materials, which can have subterahertz-operating frequencies, typically require extremely low temperatures [15]; and

(3) many of the other candidates are metallic structures wherein the electron motion induced by the electromagnetic waves near the surface of the magnet prevents the interior of the sample from interacting with the wave [16].

To circumvent these problems, various techniques have been employed or investigated. These include using materials with high anisotropy, such as barium-doped hexagonal ferrites [17–19] or using thin metallic films where eddy current damping is minimized [14,20].

More recently, the emergence of artificial materials designed for novel electromagnetic wave propagation, known as metamaterials [21], has enabled completely new solutions to this problem. The term metamaterial was initially used to describe electromagnetic structures that possess both negative permittivity and negative permeability [22]—also known as left-handed metamaterials [21]. However, it has now become a synonym of artificial structures engineered to have specific physical properties in just about any field [23]. For instance, different metamaterial designs have been recently used to make advances in topics, such as thermal-controlled chirality [24] and near-perfect light absorption [25]. In magnetism, for instance, it was recently shown that constructing metamaterials comprising canted antiferromagnetically aligned layers [26] could enable novel high-frequency microwave devices. In addition, by using ultrathin films which have operating frequencies [27] above 50 GHz due to exchange spin-wave resonances [28]. Nonetheless, these newer classes of materials either have frequencies typically below 50 GHz, require significant precision in manufacturing, or have nonreciprocal effects which are relatively small.

*Rair.Macedo@glasgow.ac.uk

 

In contrast, in this paper we show that by structuring thicker magnetic metallic films into a magnetic grating, it is possible to considerably reduce the conductivity of the overall structure as well as to engineer strong nonreciprocal responses across a wide range of frequencies. A particularly exciting feature that we demonstrate is nonreciprocal behavior at frequencies well above 300 GHz for these structured metallic systems. This is quite surprising since metallic ferromagnets typically have resonances in the 10–25-GHz range.

We demonstrate our findings through attenuated total reflection (ATR) calculations. We show that the frequency regions of high absorption and significant nonreciprocity can be substantially modified by changing the filling fraction of grating. To understand the reflectivity results, we calculate the dispersion relation of magnetic polariton modes of an insulator/structured metal/insulator structure and connect their spatial profiles to the nonreciprocal reflectivity spectra.

## II. THEORETICAL CALCULATIONS

We will soon discuss results for reflectivity (with a particular focus on ATR) as well as nonreciprocity of magnon modes, but before discussing our main findings, we will discuss the structure of interest as well as the main aspects of the electromagnetic theory through which we model reflectivity.

### A. The magnetic grating

Here, we will investigate the case of a structured magnetic metallic film. The structuring takes form of a supercell of a binary grating consisting of iron nanobars separated by a dielectric as shown in Fig. 1(a). This structuring method has been employed to construct a variety of metamaterials; this method has been more prominently in the field of metasurfaces where either plasmonic or phononic structures have been engineered to control reflection [29], transmission [30], and the phase profiles of electromagnetic waves [31] at various frequencies.

The width of the individual metallic strips is $d_1$, and the width of the dielectric strips is $d_2$. The parameters of the nanostructured metal film include a thickness ($d$) and the period of the grating ($\Lambda = d_1 + d_2$). The dielectric tensors for the dielectric strips and the dielectric substrate are diagonal and have relative values of $\varepsilon_d$ and $\varepsilon_s$, respectively. The dielectric tensor for the metal film composing the grating is also diagonal and is denoted by $\varepsilon_m$.

We can regard the nanostructured metal films as an effective medium when the period of the one-dimensional nanostructures is smaller than a wavelength or a decay length. In the effective-medium approximation, the graded material (the nanostructured metal film) is replaced by an effective medium having a permittivity tensor which depends upon the fraction of the material which is dielectric versus metallic. The resulting ATR reflectance calculations are straightforward. However, the effective-medium approximation makes use of the assumption that the amplitudes of the **E** and **B** fields do not vary substantially across an individual material. We note that this approximation eliminates any features that arise from the periodicity of the material including the introduction of band gaps or the shifting of wave vectors by reciprocal lattice vectors. Nonetheless, this approximation can work quite well as we showed in a previous work comparing effective-medium grating results to those found for a full expansion of the periodic solutions in each region [32].

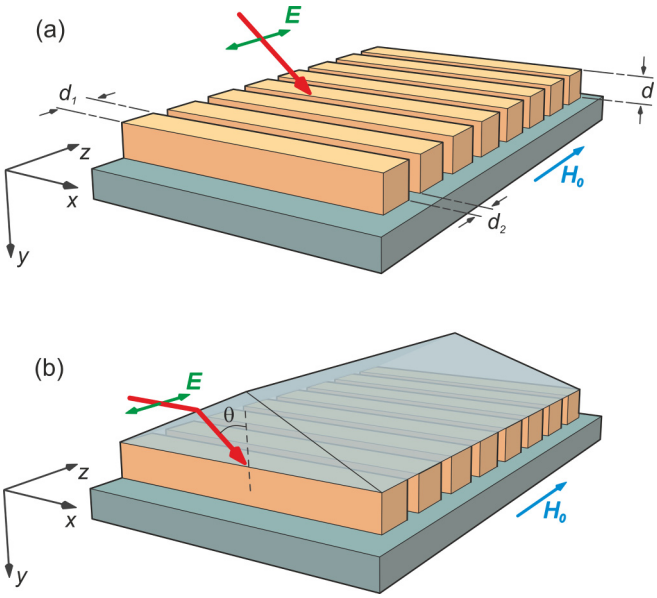


FIG. 1. (a) Geometry of a nanostructured magnetic film of thickness $d$ where the individual stripes have width $d_1$ and spaced by $d_2$. The geometry of the incident electromagnetic wave is also shown; a TE-polarized incident beam whose $E$ field is directed along $z$ and perpendicular to the structuring direction. (b) Illustration of the Kretschmann ATR geometry with the magnetic grating, static applied field $\mathbf{H}_0$, and the coordinate axes. The incident wave (also TE-polarized) is at an angle $\theta$ with respect to the surface normal inside a dielectric prism.

An effective-medium approximation is used, appropriate for the orientation of the electric-field component being perpendicular with respect to the grating in the metal film. The dielectric constants for the metal and the dielectric spacers in the grating are $\varepsilon_m$ and $\varepsilon_d$, respectively. The effective-medium dielectric tensor $\overleftrightarrow{\varepsilon}(\omega)$ appropriate for the geometry in Fig. 1 is given by

$$\overleftrightarrow{\varepsilon}(\omega) = \begin{pmatrix} \varepsilon_{xx} & 0 & 0 \\ 0 & \varepsilon_{yy} & 0 \\ 0 & 0 & \varepsilon_{zz} \end{pmatrix} = \begin{pmatrix} f_m\varepsilon_m + f_d\varepsilon_d & 0 & 0 \\ 0 & f_m\varepsilon_m + f_d\varepsilon_d & 0 \\ 0 & 0 & \left(\frac{f_m}{\varepsilon_m} + \frac{f_d}{\varepsilon_d}\right)^{-1} \end{pmatrix}, \tag{1}$$

where $f_m$ is the fraction of the film made up of the metallic magnetic material and is given by

$$f_m = \frac{d_1}{d_1 + d_2}. \tag{2}$$

Similarly, $f_d$ is the fraction of the film made up of the dielectric material and is given by

$$f_d = \frac{d_2}{d_1 + d_2}. \tag{3}$$

The frequency-dependent magnetic permeability tensor for the metallic material has the form

$$\overleftrightarrow{\mu}(\omega) = \begin{pmatrix} \mu_{xx} & \mu_{xy} & 0 \\ \mu_{yx} & \mu_{yy} & 0 \\ 0 & 0 & 1 \end{pmatrix}, \tag{4}$$

with the relevant components for a typical ferromagnetic material listed in the Methods section. The dielectric fill material and the substrate are both nonmagnetic and have a permeability of unity. The permeability tensor for the effective medium representing the nanostructured metal film is as follows:

$$\begin{aligned} \overleftrightarrow{\mu}(\omega) &= \begin{pmatrix} \mu_1 & i\mu_2 & 0 \\ -i\mu_2 & \mu_1 & 0 \\ 0 & 0 & 1 \end{pmatrix} \\ &= \begin{pmatrix} f_m\mu_{xx} + f_d & f_m\mu_{xy} & 0 \\ f_m\mu_{yx} & f_m\mu_{yy} + f_d & 0 \\ 0 & 0 & 1 \end{pmatrix}. \end{aligned} \tag{5}$$

### B. Attenuated total reflection off a magnetic grating

The ATR geometry used to probe the electromagnetic response of the magnetic grating is illustrated in Fig. 1(b). A high index of refraction prism with permittivity denoted by $\varepsilon_p$ is used in the Kretschmann configuration [33] to increase the momentum of the incident photons. The structured metallic film is placed on the base of the prism with no intermediate layer between the film and prism. We also consider that the film is grown on a dielectric substrate with permittivity $\varepsilon_s$. The incident electromagnetic radiation has an angular frequency $\omega$, and the electric field is in the $z$ direction and always parallel to the surface and perpendicular to the nanobars.

To find the reflectivity coefficient, one first assumes a wavelike behavior in each region. We assume that the incident wave is transverse electric (TE) polarized with $\mathbf{E}$ directed along the $z$ direction. Thus, the $\mathbf{E}$ field in each of the three regions can be written as

$$\mathbf{E}_1(\mathbf{x}, t) = [a_1 e^{ik_{1\perp}(y)} + b_1 e^{-ik_{1\perp}(y)}] e^{i(k_\parallel x - \omega t)} \hat{\mathbf{z}}, \tag{6}$$

in the prism (first region),

$$\mathbf{E}_2(\mathbf{x}, t) = [a_2 e^{ik_{2\perp}(y)} + b_2 e^{-ik_{2\perp}(y)}] e^{i(k_\parallel x - \omega t)} \hat{\mathbf{z}}, \tag{7}$$

in the effective medium (second region) and

$$\mathbf{E}_3(\mathbf{x}, t) = a_3 e^{ik_{3\perp}(y)} e^{i(k_\parallel x - \omega t)} \hat{\mathbf{z}}, \tag{8}$$

in the substrate (third region).

The parallel component of the wave-vector $k_\parallel = \frac{\omega}{c}\sqrt{\varepsilon_p}\sin\theta$ is constant in all three regions, and the perpendicular components are determined by using the dispersion relation for each medium separately. One finds

$$k_{1\perp}^2 = \left(\frac{\omega}{c}\right)^2 \epsilon_p - k_\parallel^2, \tag{9}$$

$$k_{2\perp}^2 = \left(\frac{\mu_1^2 - \mu_2^2}{\mu_1}\right)\left(\frac{\omega}{c}\right)^2 \epsilon_{zz} - k_\parallel^2, \tag{10}$$

and

$$k_{3\perp}^2 = \left(\frac{\omega}{c}\right)^2 \epsilon_d - k_\parallel^2. \tag{11}$$

To find the reflectance, one must also satisfy the boundary conditions at each surface. We, thus, require that $H_x$ and the tangential component of $\mathbf{E}$ be continuous at the interfaces. Since we know the $\mathbf{E}$ field from Eqs. (6)–(8), the $\mathbf{H}$ field associated with each of the electric fields is found by applying Maxwell's equations. By use of $\nabla \times \mathbf{E} = -\frac{\partial \mathbf{B}}{\partial t}$ and $\mathbf{B} = \mu_0 \overleftrightarrow{\mu}(\omega)\mathbf{H}$ a general relationship between $\mathbf{E}$ and $H_x$ for this problem is found to be as follows:

$$H_x(\mathbf{x}, t) = \frac{c}{i\omega\left(\mu_1^2 - \mu_2^2\right)}\left[\mu_1 \frac{\partial \mathbf{E}}{\partial y} + i\mu_2 \frac{\partial \mathbf{E}}{\partial x}\right]. \tag{12}$$

Note that this is the most general case—that of the structured grating where $\overleftrightarrow{\mu}(\omega)$ is given by Eq. (5). However, Eq. (12) also applies to the other layers; as these layers are dielectric, for them we can simply make $\mu_1 = 1$ and $\mu_2 = 0$. Continuity of tangential $\mathbf{E}$ and $H_x$ at $y = 0$ (the boundary between the prism and the effective medium grating so that $\mathbf{E}_1 = \mathbf{E}_2$ and $H_{1x} = H_{2x}$) yield the following two equations:

$$a_1 = -b_1 + a_2 + b_2, \tag{13}$$

and

$$a_1 k_{1\perp} = b_1 k_{1\perp} + a_2 k_+ + b_2 k_-, \tag{14}$$

where

$$k_\pm = \frac{ik_x\mu_2 \pm k_{2\perp}\mu_1}{\mu_1^2 - \mu_2^2}. \tag{15}$$

Similarly, continuity of $\mathbf{E}$ and $H_x$ at $y = d$ (the boundary between the effective-medium grating and the substrate so that $\mathbf{E}_2 = \mathbf{E}_3$ and $H_{2x} = H_{3x}$) results in the two following equations:

$$a_2 e^{ik_{2\perp}d} + b_2 e^{-ik_{2\perp}d} - a_3 e^{ik_{3\perp}d} = 0, \tag{16}$$

and

$$a_2 k_+ e^{ik_{2\perp}d} + b_2 k_- e^{-ik_{2\perp}d} - a_3 k_{3\perp} e^{ik_{3\perp}d} = 0. \tag{17}$$

This system of four equations and four unknowns is easily solved numerically for the reflectance by setting the variable $a_1$ equal to one and finding the ATR signal by $|b_2|^2$.

## III. RESULTS

Unless otherwise indicated, the parameters for our calculations are as follows. The dielectric medium that fills the grating nanoslits has an index of refraction of 1.333. This value is typical of water as might be found in a biosensing application, but this is also a typical value for Teflon which is widely employed in microwave devices [34]. There is a dielectric medium below the film again with $n = 1.333$—corresponding to $\varepsilon_d = \varepsilon_s = n^2$. We consider TE polarized incident light with frequencies that vary from 3 to 350 GHz at incident angle $\theta$, and we take the speed of light to be $c = 3.0\times10^{10}$ cm s$^{-1}$. The refractive index of the prism is 1.723 (SF10 glass) [35] and the electrical permittivity of

the metal is frequency dependent: $\varepsilon_m = 1 + \frac{i\sigma}{\varepsilon_0 \omega}$; with $\sigma = 1.02\times10^7$ S m$^{-1}$, which is appropriate for iron, and the permittivity of free space is $\varepsilon_0 = 8.85\times10^{12}$ F m$^{-1}$.

Before detailing our main findings, we first note that for our geometry for reflectivity we only require $\varepsilon_{zz}$ [see Eq. (1)], which from here onward, we will simply refer to as the effective dielectric constant of the grating structure $\varepsilon_{\text{eff}}$. This constant varies significantly with the filling factors following the relation:

$$\frac{1}{\varepsilon_{\text{eff}}} = \frac{f_m}{\varepsilon_m} + \frac{f_d}{\varepsilon_d}. \tag{18}$$

But since the metal has a very high $\varepsilon_m$, this reduces to a simple equation where

$$\varepsilon_{\text{eff}} \approx \frac{\epsilon_d}{f_d}. \tag{19}$$

A critical value of $f_d$ occurs when $\varepsilon_{\text{eff}} > \varepsilon_p$. Values above this are in the "fiber optic" limit in the sense that the grating region has a higher index of refraction compared to the surrounding regions of the prism or substrate. (We note that having an index of refraction in a glasslike fiber that is larger than the index of refraction in the surrounding material leads to total internal reflection of an electromagnetic wave in the fiber with an evanescent wave outside the fiber [36,37]. We will see similar behavior in our system.) Substituting the parameters listed above, this gives

$$f_d = \frac{\varepsilon_d}{\varepsilon_p} = \frac{1.776}{2.968} = 0.60, \tag{20}$$

and the critical value for the metal filling fraction is $f_m = 0.40$.

### A. Reflectivity off an all-dielectric structure

To create the proper context, we find it useful to first investigate the case where there is no magnetic response in the grating. For this, we examine results for ATR-like measurements from a purely dielectric structure, such as that shown in Fig. 1(b) when the relative magnetic permeability tensor is artificially set to the unit matrix. In Fig. 2(a) we show the ATR results, color maps of the reflectance as a function of incident angle and frequency for the purely dielectric structure (prism/grating structure/substrate) where the metallic portion of the grating is nonmagnetic. The metallic filling fraction in the grating structure is $f_m = 0.61$, and the thickness of the effective-medium film is 0.1 cm. Furthermore, the dielectric materials are, initially, taken to have wholly real values for their dielectric constants. We see two distinct regions: a reflectivity of unity (red) for angles beyond $= 50.6°$, and a low reflectivity for angles below 50.6°. If one calculates the critical angle between the high-index prism and the low-index substrate, it is found to be 50.6° [this is shown as the vertical dashed lines in Figs. 2(a) and 2(b)]. For angles below this value, one does not have total internal reflection and, hence, the central region in the ATR curves generally corresponds to lowered transmission.

Figure 2(b) expands the situation by adding a small imaginary portion to the dielectric constant of the substrate material allowing the incident radiation to couple to surface modes, i.e., $\varepsilon_s = 1.333^2 + 0.5i$. In addition to the features described above, there are now narrow fingers of reduced reflectivity extending beyond the central region. As we will see later, these correspond to fiber opticlike states where the grating region has a higher index of refraction compared to the surrounding regions of the prism or substrate [36]. Much like surface polaritons, these fiber opticlike states (also known as guided waves) interact with the incident wave only at certain frequencies where they can exist—here related to the thickness on the film or its dielectric constant—so that the reflectivity dips almost to zero. Basically, in the regions where the fiber optic states can exist, they carry off the energy of the incident radiation, resulting in a reduction in the reflectivity. We note that all of the results are strictly reciprocal, i.e., the reflectivity for the positive and negative values of the incident angle is identical.

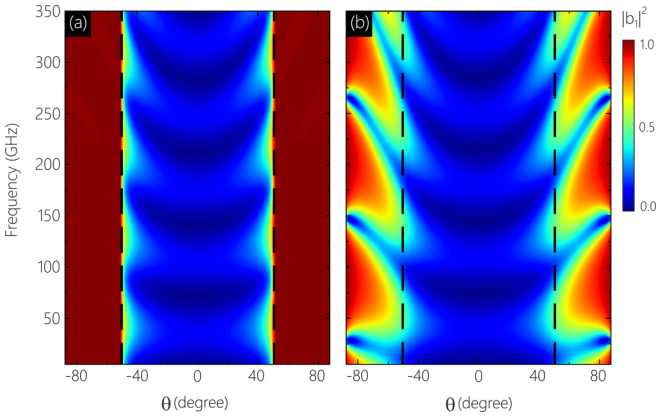


FIG. 2. (a) ATR spectra maps showing the reflectance as a function of incident angle and frequency. The overlayer has a dielectric constant of $\varepsilon_p = 2.968$ and the substrate's is $\varepsilon_s = 1.33$. The middle layer takes the effective dielectric constant of the metallic grating $\varepsilon_{\text{eff}}$, albeit being nonmagnetic [so that $\overleftrightarrow{\mu}(\omega) = 1$]. Here, $f_m = 0.61$, and $d = 0.1$ cm. Note that all three dielectric constants are purely real, and in (b) we show the effect of damping by making the dielectric constant of the substrate $\varepsilon_3 = 1.33 + 0.5i$.

### B. Reflectivity off a magnetic grating

In Fig. 3 we show results for the case where the magnetic response in the grating is turned back on, but we keep the same dielectric parameters as those used in Fig. 2(b). There are substantial differences between Figs. 2(b) and 3. First, all the reflectance map is now significantly nonreciprocal. This is most evident in the frequency range of 30–80 GHz where there is a distinct fingerlike feature for negative angles and no corresponding feature on the right. However, there are other nonreciprocal features as well. If we look at the black-dashed horizontal line marking the 150-GHz position, it is easy to see that the results for positive, and negative angles are not the same with the features on the left side being shifted up by about 10 GHz compared to the similar features on the right side. As one goes higher in frequency, the nonreciprocity becomes smaller but is still present throughout.

In Fig. 4 we explore how the ATR behavior changes as a function of the magnetic filling fraction $f_1$. There are several interesting features which can be seen in Fig. 4:

(1) Again, there is a central region ($|\theta| < 50.6°$) where the reflectivity is low, corresponding to angles below the

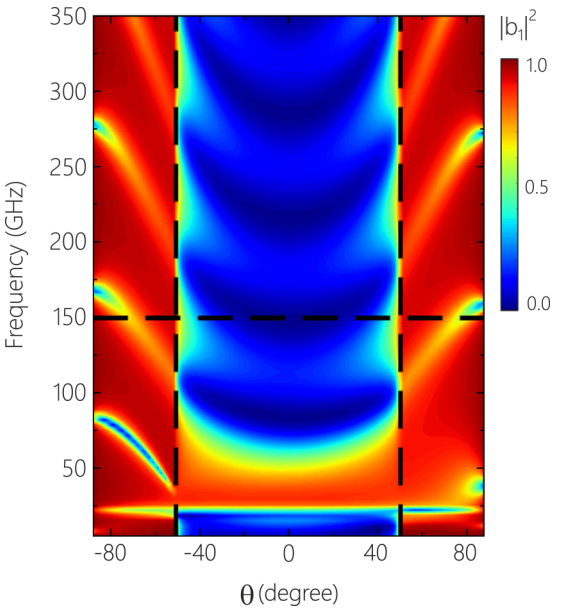


FIG. 3. ATR spectra map for the same dielectric parameters as 3(b) except now the magnetic permeability is also included [according to Eq. (5)]. We note the distinct nonreciprocity in the reflectivity for $|\theta| > 50^\circ$ at frequencies ranging from about 30–80 GHz. Using the horizontal black line, as a guide, at 150 GHz we can see there is also substantial nonreciprocity even at that frequency.

critical angle as described above. The exceptions to this are where the magnetic material has a stop band, i.e., a frequency region where no electromagnetic waves propagate. In this case the frequency range of the stop band depends on the filling fraction. At low filling fractions the stop band is restricted to values near $f = \mu_0\gamma\sqrt{H(H+M)} = 29$ GHz, for larger values of the filling fraction, the magnetic stop band extends up to the so-called antiresonance frequency [38] of $f = \mu_0\gamma(H+M) = 74.5$ GHz for the parameters used here.

(2) For some filling fraction values there is a strong nonreciprocity in reflection that extends from about 25 GHz to over 120 GHz.

(3) The distinctive bands of nonreciprocity are primarily seen at incident angles above approximately 50°; although some nonreciprocal behavior also is seen at smaller incident angles for some frequency ranges.

(4) At low filling fractions, there is a large region where the reflectivity is nearly zero. As the filling fraction increases, this breaks up into individual bands of low reflectivity. This is primarily due to the dielectric response of the medium as indicated in Fig. 2.

(5) We should also mention that the positions of the nonreciprocal features are tunable with the applied magnetic field. For example, decreasing the external field from 0.6 to 0.2 T shifts the nonreciprocal ranges down in frequency by 10 GHz.

### C. Dispersion Relation for Bound Polaritons

To understand the ATR results, it is helpful to calculate the polariton modes that exist in our effective-medium film surrounded by two different dielectrics as shown in Fig. 5. The investigation of the TE-polarized polaritons is performed by determining the dispersion relation in the film and the surrounding dielectric materials, which is then used with the surface boundary conditions to determine the wave profiles for the bound polaritons. Because this calculation is similar to the ATR calculation described earlier, we only give a brief outline.

Again, one first assumes a wavelike behavior in each region around the film with the **E** field only in the $z$ direction as shown in Fig. 2. The electric fields are given by

$$\mathbf{E}(\mathbf{x},t) = \mathcal{A}e^{+\alpha(y)}e^{i(k_\parallel x-\omega t)}\hat{\mathbf{z}} \quad \text{for } y < 0, \tag{21}$$

$$\mathbf{E}(\mathbf{x},t) = [\mathcal{B}e^{ik_{2\perp}(y)} + \mathcal{C}e^{-ik_{2\perp}(y)}]e^{i(k_\parallel x-\omega t)}\hat{\mathbf{z}} \quad \text{for } 0 < y < d, \tag{22}$$

and

$$\mathbf{E}(\mathbf{x},t) = \mathcal{D}e^{-\beta(y)}e^{i(k_\parallel x-\omega t)}\hat{\mathbf{z}} \quad \text{for } y > d. \tag{23}$$

The values of $\alpha$ and $\beta$ can be obtained from Eqs. (9) and (11) by making $\alpha = ik_{1\perp}$ and $\beta = ik_{3\perp}$, and we assume that the real parts of $\alpha$ and $\beta$ are positive.

To find the dispersion of the polariton, one must also satisfy the boundary conditions at each surface. We, thus, require that $H_x$ and the tangential component of **E** be continuous at the interfaces. Continuity of tangential **E** at $y = 0$ and $y = +d$ gives the following two equations:

$$\mathcal{A} - \mathcal{B} - \mathcal{C} = 0, \tag{24}$$

and

$$\mathcal{B}e^{ik_{2\perp}d} + \mathcal{C}e^{-ik_{2\perp}d} - \mathcal{D}e^{-\beta d} = 0. \tag{25}$$

Similarly, continuity of $H_x$ at each of the boundaries results in the two following equations:

$$k_{1\perp}\mathcal{A} - k_-\mathcal{B} + k_+\mathcal{C} = 0, \tag{26}$$

and

$$k_-e^{ik_{2\perp}d}\mathcal{B} - k_+e^{-ik_{2\perp}d}\mathcal{C} + \beta e^{-\beta d}\mathcal{D} = 0, \tag{27}$$

again where $k_\pm$ is given by Eq. (15).

Equations (24)–(27) are a homogeneous set of equations for the variables $\mathcal{A}$–$\mathcal{D}$. When put in matrix form, the determinant matrix $\mathfrak{M}$ must be zero for a nontrivial solution. The solutions can be found in a number of ways. First one can plot the $\log_{10}(|\mathfrak{M}|)$ as a function of $\mathrm{Re}(k_\parallel)$ and $\omega$ as a color map. Smaller values for $\log_{10}(|\mathfrak{M}|)$ give the positions for the dispersion relation of bound polaritons of this three-layer system. To obtain the exact values, i.e., both $\mathrm{Re}(k_\parallel)$ and $\mathrm{Im}(k_\parallel)$, one must use a complex root finder.

To find the wave profiles, one uses the values of frequency and wave vector in the boundary conditions to find, for example, $\mathcal{A}$–$\mathcal{C}$ in terms of $\mathcal{D}$. This allows one to plot the wave profile for different locations along the dispersion curve.

To place the results for the magnetic material in context, we again start by presenting the numerical results for the dispersion relation for the dielectric-only version of this problem (so $H_0 = 0$ in Fig. 5 and the permeability tensor is again set to the unit matrix). The parameters here are the same as those in Fig. 3, namely, $f_m = 0.61$ and $\varepsilon_s = 1.333^2 + 0.5i$.

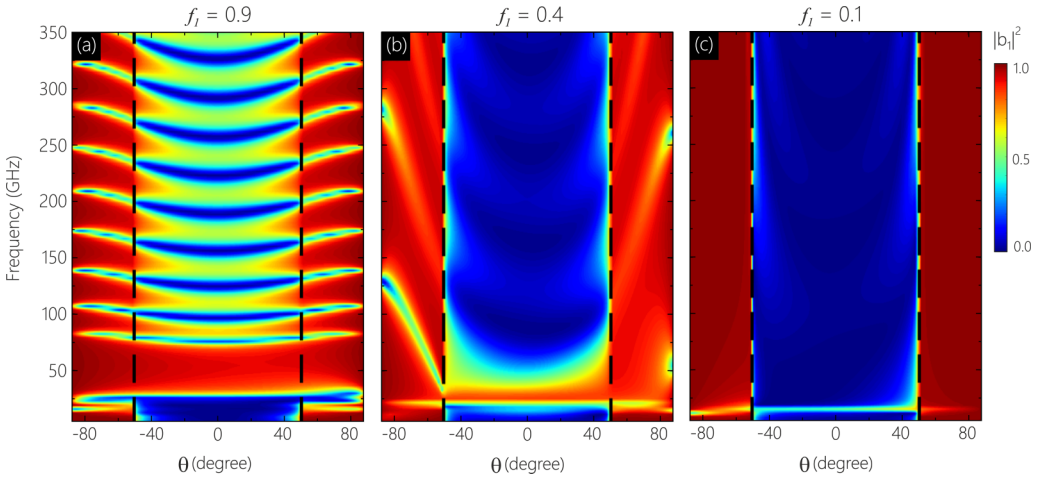


FIG. 4. ATR spectra maps for different values of the filling factor, $f_1$. The color bar on the right gives the reflectance values, which in the maps are plotted as a function of both the incident angle and the frequency. The specific parameters for these plots are $\mu_0 H_0 = 0.4$ T, $d = 0.1$ cm, $\alpha = 0.02$. The dielectric parameters for all layers are those of Fig. 2(b).

The dispersion relations and mode profiles for several bound states are shown in Fig. 6. In part (a), the dashed black lines indicate the boundary for what features are visible in the ATR measurement, i.e., incident angles less than 90° with dispersion curves inside (lower angles), the boundary line visible in ATR, and those outside are not seen. The solid black lines and respective shaded region in the center indicate the region where propagation should take place as the combination of incident angle and dielectric constant of the substrate do not allow for confinement of waves. The results agree well with what is seen in the ATR spectrum of Fig. 2(b) where there are narrow regions of low reflectivity at higher angles from 20–30 GHz and again for frequencies of 100–160 GHz and just above 250 GHz. These low reflectivity regions can, in fact, be traced to the modes (white solid lines) as the frequencies where each mode meets the prism's light line (dashed black line). In other words, the incident radiation is being effectively transferred to a surface or bound polariton with a resultant loss in reflectivity.

We can obtain insight into the nature of the modes by plotting the profiles of the various modes as seen in Figs. 6(b)–6(d). The modes have an oscillator behavior in the central region (grating), but the wave decays to zero outside that region. We note that the waves are reciprocal in that the profiles for $+\mathbf{k}$ and $-\mathbf{k}$ are identical.

When the magnetic response in the grating is included, the dispersion relations change significantly as is expected from the ATR results in Fig. 3 and as seen in Fig. 7. The dispersion relations for the lowest-frequency modes show substantial nonreciprocity with values for the $-\mathbf{k}$ side lying inside the region probed by ATR and the values for the $+\mathbf{k}$ side lying mostly outside the boundary. This is exactly the behavior found in Fig. 3 where there is strong nonreciprocity for the features seen in the 30–70-GHz range.

A surprising feature of the ATR and dispersion relation results is the large frequency range where there is significant nonreciprocal behavior. For *magnetostatic* waves nonreciprocity occurs as a result of the off-diagonal terms in the permeability, $\mu_{xy}$ *or* $\mu_{yx}$ [39]. Furthermore, for magnetostatic waves, nonreciprocity is confined to the frequency region where $\mu_{xx}$ is negative because for these frequencies bulk waves are forbidden [40], and one finds nonreciprocal surface waves. In contrast, in the fully retarded electromag-

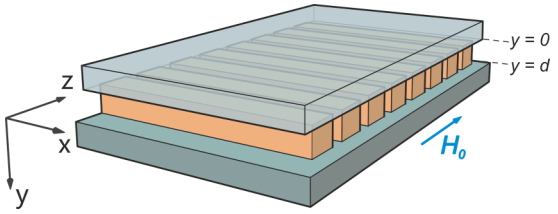


FIG. 5. Geometry used for the calculation of the dispersion relation for bound polaritons.

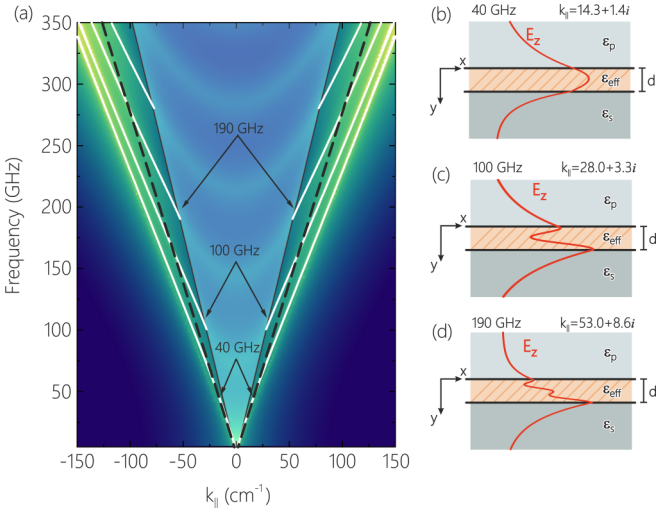


FIG. 6. (a) Dispersion relations for bound polariton states in the three-layer geometry when the effective medium is not magnetic. The color map presents the $\log_{10}(|\mathcal{M}|)$ as a function of $\mathrm{Re}(k_\parallel)$ and $\omega$ as discussed in the text. (b)–(d) Profiles of guided waves at different frequencies.

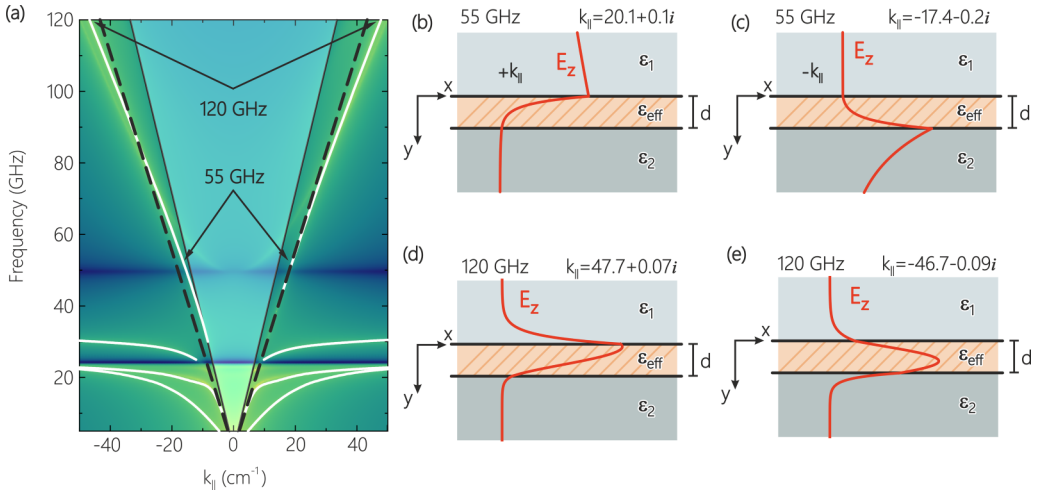


FIG. 7. (a) Dispersion relations for bound polariton states in the three-layer geometry with the magnetic metallic material. The color map presents the $\log_{10}(|\mathfrak{M}|)$ as a function of $\mathrm{Re}(k_\parallel)$ and $\omega$ as discussed in the text. (b)–(e) polariton profiles which are different.

netic system discussed here, we find that surface waves, or bound states, appear even in the absence of a magnetic material as seen in Figs. 2 and 6. Therefore, there is no requirement for the diagonal component of the permeability tensor to be negative in order to have surfacelike waves. However, a nonzero value for the off-diagonal components of the permeability is still required to have nonreciprocity.

In Figs. 7(b) and 7(c) we show the mode profiles at 55 GHz which are drastically different from those of the purely dielectric case (in Fig. 6). Here the bound waves are evanescent inside the grating as well as outside—which is distinct feature of true surface waves, in this case, surface magnon polaritons. For the parameters used here, the region where these modes are found extends from region extends from about 25 to 50 GHz.

We find interesting to note, however, that these surface modes seem to continue to exist at high frequencies (looking at the white solid lines starting around 30–40 GHz, they continue on towards the 100s of gigahertz). Although it looks like the same mode, its character changes as it moves off the region where the permeability is negative. In Figs. 7(d) and 7(e) we show its behavior at 120 GHz where a distinct oscillating behavior is now seen inside the material.

As we have stated, the nonreciprocity is not confined to the region where the permeability is negative. As we have seen in the reflectivity, we get large nonreciprocity over a much larger frequency region, extending easily up to 300 GHz. This is still an effect of the off-diagonal component of the permeability which albeit small, it is still present up to and beyond 300 GHz. We should note that the nonreciprocity in the dispersion relations is reduced, however, as the frequency increases, and the effect of the off-diagonal components become less dominant. We have omitted the dispersion curves for higher frequencies for the magnetic grating as the general behavior is very similar to that shown in Fig. 6, but nonetheless there is a significant difference in the dispersion relations which is manifested in a nonreciprocal reflection seen in Fig. 3.

## IV. DISCUSSION AND CONCLUSIONS

We have demonstrated nonreciprocal behavior over a large frequency range, extending up to 300 GHz, will occur in attenuated total reflection measurements with a magnetic grating as the active element. The grating is composed of a moderately thick magnetic metallic film, separated by thin insulating sections. This reduces the conductivity of the overall structure, and we obtain strong nonreciprocal electromagnetic responses at high frequencies.

A way to realize the structures that we discuss here, is to use focused ion beam (FIB) techniques which can be used to cut, slice, and drill magnetic samples [41,42]. For effective-medium theory to be appropriate, one wants the overall change in the fields to be small over the length of a unit cell. In this problem, the metallic skin depth—typically on the order of a few microns—sets the length scale for the size of a unit cell. Because FIB systems can make cuts with dimensions as low as a few nanometers, it should be possible to fabricate appropriate unit cells with a variety of fill factors.

We show that the frequency regions of high absorption and significant nonreciprocity can be substantially modified by changing the filling fraction of the grating. By calculating the dispersion relations of the magnetic polariton modes of an insulator/grooved metal/ insulator structure and connecting their spatial profiles to the nonreciprocal reflectivity results we are able to understand the reflectivity results. The drivers for the nonreciprocal behavior are the off-diagonal components of the permeability tensor which are present up to and beyond 300 GHz, and the presence of surface (or bound polariton) modes which result from the dielectric properties of the grating.

These findings could be verified experimentally through a variety of techniques, including standard reflectivity or ATR measurements. For example, reflectivity experiments in the 200–300-GHz range have been developed for antiferromagnetic crystals where the incident radiation is created by a third harmonic wave generated from an impatt diode with fundamental frequency at 88 GHz [43]. At lower frequencies, we

expect that the metamaterial should be easy to incorporate into microwave waveguide structures where the electromagnetic behavior can be probed. The lowered conductivity should lead to much stronger responses than that of conventional continuous metallic films. Finally, it is noted that in addition to the magnetic material filling fraction and overall metamaterial thickness the positions of the nonreciprocal features can be tuned with the applied magnetic field.

## V. METHODS

*Permeability tensor and parameters for the magnetic material*: The permeability tensor for the magnetic material is given by the following:

$$\mu = \begin{pmatrix} \mu_{xx} & \mu_{xy} & 0 \\ \mu_{yx} & \mu_{yy} & 0 \\ 0 & 0 & 1 \end{pmatrix}.$$

Here

$$\mu_{xx} = \mu_{yy} = 1 + \frac{\omega_M[\omega_H(1+\alpha^2) - i\omega\alpha]}{\omega_H^2(1+\alpha^2) - 2i\omega\alpha\omega_H - \omega^2},$$

and

$$\mu_{xy} = -\mu_{yx} = i\,\frac{\omega_M\omega}{\omega_H^2(1+\alpha^2) - 2i\omega\alpha\omega_H - \omega^2}.$$

The terms in these equations are as follows:

$$\omega_M = \gamma\mu_0 M,$$
$$\omega_H = \gamma\mu_0 H_0.$$

Here the gyromagnetic ratio is $\gamma = 2\pi \times 29$ GHz T$^{-1}$. The magnetization, $\mu_0 M = 2.17$ T, appropriate for iron and the applied field $\mu_0 H_0 = 0.4$ T unless otherwise noted. The Gilbert damping parameter $\alpha$ has the values denoted in the text.


[1] C. L. Hogan, The ferromagnetic faraday effect at microwave frequencies and its applications: The microwave gyrator, Bell Syst. Tech. J. **31**, 1 (1952).

[2] C. L. Hogan, The ferromagnetic faraday effect at microwave frequencies and its applications, Rev. Mod. Phys. **25**, 253 (1953).

[3] G. H. B. Thompson, Unusual waveguide characteristics associated with the apparent negative permeability obtainable in ferrites, Nature (London) **175**, 1135 (1955).

[4] R. Zivieri, Dynamic Negative Permeability in a Lossless Ferromagnetic Medium, in *9th International Congress on Advanced Electromagnetic Materials in Microwaves and Optics (METAMATERIALS)* (IEEE, Piscataway, NJ, 2015), p. 532.

[5] R. Zivieri, Dynamic Permeability in a Dissipative Ferromagnetic Medium, in *10th International Congress on Advanced Electromagnetic Materials in Microwaves and Optics (METAMATERIALS)* (IEEE, Piscataway, NJ, 2016), p. 427.

[6] B. K. Kuanr, V. Veerakumar, R. Marson, S. R. Mishra, R. E. Camley, and Z. Celinski, Nonreciprocal microwave devices based on magnetic nanowires, Appl. Phys. Lett. **94**, 202505 (2009).

[7] V. Cherepanov, I. Kolokolov, and V. L'vov, The saga of YIG: Spectra, thermodynamics, interaction and relaxation of magnons in a complex magnet, Phys. Rep. **229**, 81 (1993).

[8] V. G. Harris *et al.*, Recent advances in processing and applications of microwave ferrites, J. Magn. Magn. Mater. **321**, 2035 (2009).

[9] M. Giordani, M. Polese, M. Mezzavilla, S. Rangan, and M. Zorzi, Toward 6g networks: Use cases and technologies, IEEE Commun. Mag. **58**, 55 (2020).

[10] T. Huang, W. Yang, J. Wu, J. Ma, X. Zhang, and D. Zhang, A survey on green 6g network: Architecture and technologies, IEEE Access **7**, 175758 (2019).

[11] S. Yuan, L. Chen, Z. Wang *et al.*, On-chip terahertz isolator with ultrahigh isolation ratios, Nat. Commun. **12**, 5570 (2021).

[12] B. Heydari, M. Bohsali, E. Adabi, and A. M. Niknejad, Millimeter-wave devices and circuit blocks up to 104 GHz in 90 nm CMOS, IEEE J. Solid-State Circuits **42**, 2893 (2007).

[13] J. Zhao, C. Li, X. Li, and L. Shen, Technical challenges for high-frequency wireless communication, J. Commun. Inf. Networks **1**, 19 (2016).

[14] B. Kuanr, Z. Celinski, and R. E. Camley, Tunable high-frequency band-stop magnetic filters, Appl. Phys. Lett. **83**, 3969 (2003).

[15] R. Macêdo, in *Tunable Hyperbolic Media: Magnon-Polaritons in Canted Antiferromagnets*, edited by R. E. Camley and R. L. Stamps, Solid State Physics (Academic Press, Burlington, VT, 2017), Vol. 68, Chap. 2, pp. 91–155.

[16] R. G. Chambers, Anomalous skin effect in metals, Nature (London) **165**, 239 (1950).

[17] T. J. Fal and R. E. Camley, Hexagonal ferrites for use in microwave notch filters and phase shifters, J. Appl. Phys. **104**, 23910 (2008).

[18] Z. Wang *et al.*, Millimeter wave phase shifter based on ferromagnetic resonance in a hexagonal barium ferrite thin film, Appl. Phys. Lett. **97**, 72509 (2010).

[19] Y. Y. Song, J. Das, Z. Wang, W. Tong, and C. E. Patton, In-plane c-axis oriented barium ferrite films with self-bias and low microwave loss, Appl. Phys. Lett. **93**, 172503 (2008).

[20] E. Salahun, P. Quéffélec, G. Tanné, A. L. Adenot, and O. Acher, Correlation between magnetic properties of layered ferromagnetic/dielectric material and tunable microwave device applications, J. Appl. Phys. **91**, 5449 (2002).

[21] D. R. Smith, W. J. Padilla, D. C. Vier, S. C. Nemat-Nasser, and S. Schultz, Composite Medium with Simultaneously Negative Permeability and Permittivity, Phys. Rev. Lett. **84**, 4184 (2000).

[22] V. G. Veselago, The Electrodynamics of Substances with Simultaneously Negative Values of $\epsilon$ and $\mu$, Sov. Phys. Usp. **10**, 509 (1968).

[23] M. Kadic, G. W. Milton, M. van Hecke *et al.*, 3D metamaterials, Nat. Rev. Phys. **1**, 198 (2019).

[24] T. Lv, Y. Li, H. Ma *et al.*, Hybrid metamaterial switching for manipulating chirality based on $VO_2$ phase transition, Sci. Rep. **6**, 23186 (2016).

[25] Y. Xiang, X. Dai, J. Guo *et al.*, Critical coupling with graphene-based hyperbolic metamaterials, Sci. Rep. **4**, 5483 (2014).

[26] R. Macêdo, K. L. Livesey, and R. E. Camley, Using magnetic hyperbolic metamaterials as high frequency tunable filters, Appl. Phys. Lett. **113**, 121104 (2018).

[27] P. M. Yarbrough, K. L. Livesey, R. E. Camley, and R. Macêdo, Far-Infrared Reflection from Heterostructures Made of Ultrathin Ferromagnetic Layers, Phys. Rev. Appl. **12**, 024004 (2019).

[28] R. V. Mikhaylovskiy, E. Hendry, and V. V. Kruglyak, Negative permeability due to exchange spin-wave resonances in thin magnetic films with surface pinning, Phys. Rev. B **82**, 195446 (2010).

[29] J. Rensberg *et al.*, Active optical metasurfaces based on defect-engineered phase-transition materials, Nano Lett. **16**, 1050 (2016).

[30] K.-P. Chen, S.-C. Ye, C.-Y. Yang, Z.-H. Yang, W. Lee, and M.-G. Sun, Electrically tunable transmission of gold binary-grating metasurfaces integrated with liquid crystals, Opt. Express **24**, 16815 (2016).

[31] J. Park, J. H. Kang, S. J. Kim, X. Liu, and M. L. Brongersma, Dynamic reflection phase and polarization control in metasurfaces, Nano Lett. **17**, 407 (2017).

[32] M. H. Tyboroski, N. R. Anderson, and R. E. Camley, An effective medium study of surface plasmon polaritons in nanostructured gratings using attenuated total reflection, J. Appl. Phys. **115**, 013104 (2014).

[33] E. Kretschmann, Die Bestimmung optischer Konstanten von Metallen durch Anregung von Oberflächenplasmaschwingungen, Z. Phys. **241**, 313 (1971).

[34] V. Fedotov, Metamaterials in *Springer Handbook of Electronic and Photonic Materials*, edited by S. Kasap and P. Capper (Springer, Cham, Switzerland, 2017), p. 1.

[35] J. Bai *et al.*, Embedded optical waveguides fabricated in SF10 glass by low-repetition-rate ultrafast laser, Appl. Opt. **52**, 7288 (2013).

[36] T. Li, Structures, parameters, and transmission properties of optical fibers, Proc. IEEE **68**, 1175 (1980).

[37] C. Yeh, Guided-wave modes in cylindrical optical fibers, IEEE Trans. Educ. **E-30**, 43 (1987).

[38] B. Heinrich and V. F. Meshcheryakov, Transmission of an Electromagnetic Wave by a Ferromagnetic Metal in the Antiresonance Region, Sov. Phys. JETP **32**, 232 (1971).

[39] R. E. Camley, Nonreciprocal surface waves, Surf. Sci. Rep. **7**, 103 (1987).

[40] R. Macêdo and R. E. Camley, Engineering terahertz surface magnon-polaritons in hyperbolic antiferromagnets, Phys. Rev. B **99**, 014437 (2019).

[41] P. G. Baity, D. A. Bozhko, R. Macêdo, W. Smith, R. C. Holland, S. Danilin, V. Seferai *et al.*, Strong magnon–photon coupling with chip-integrated YIG in the zero-temperature limit, Appl. Phys. Lett. **119**, 033502 (2021).

[42] R. Macêdo, R. C. Holland, P. G. Baity, L. J. McLellan, K. L. Livesey, R. L. Stamps, M. P. Weides, and D. A. Bozhko, Electromagnetic Approach to Cavity Spintronics, Phys. Rev. Appl. **15**, 024065 (2021).

[43] L. Remer, B. Lüthi, H. Sauer, R. Geick, and R. E. Camley, Nonreciprocal Optical Reflection of the Uniaxial Antiferromagnet $MnF_2$, Phys. Rev. Lett. **56**, 2752 (1986).